https://dx.doi.org/10.1016/j.ijheatmasstransfer.2022.123092

This is the Pre-Published Version.

A multiscale model for proton exchange membrane fuel cells with order-structured catalyst layers

P.Z. Lin[a], J. Sun[a], M.C. Wu[b, *], T.S. Zhao[a, c, *]

[a] Department of Mechanical and Aerospace Engineering, The Hong Kong University of Science and Technology, Clear Water Bay, Kowloon, Hong Kong, China

[b] Department of Mechanical Engineering, The Hong Kong Polytechnic University, Hung Hom, Kowloon, Hong Kong SAR, China

[c] Guangzhou HKUST Fok Ying Tung Research Institute, Guangzhou, 511458, China

Abstract

Order-structured catalyst layers offer a promising solution to substantially reducing the Pt loading while maintaining the performance of proton exchange membrane fuel cells (PEMFCs). In this work, we develop a multiscale model to investigate the mass transport characteristics of a PEMFC with ordered catalyst layers. A Langmuir adsorption equation is proposed to describe the ionomer-Pt interfacial transport process in a local oxygen transport sub-model, which is integrated into a two-dimensional, two-phase cell-scale model. Simulations are validated against experimental data in the literature. Results show that the fuel cell with ordered catalyst layers can achieve much higher performance than that with conventional catalyst layers, due to the enhanced bulk and local oxygen transport. Moreover, both local oxygen transport resistances of ordered and conventional catalyst layers show an inverse proportional function of Pt loading, while the ordered catalyst layers exhibit a much smaller local oxygen transport resistance than their conventional counterparts. Under limiting current conditions, oxygen transport cross the ionomer-Pt interface dominates the local transport resistance, thus hindering the cell performance. The effects of pore size of the ordered catalyst layers and relative humidity on the oxygen transport characteristics and cell performance are also investigated. This work provides new insights into the mass transport mechanisms in ordered catalyst layers, which will facilitate the development of high-performance PEMFCs with low Pt loading.

Keywords: proton exchange membrane fuel cell; multiscale modeling; oxygen transport resistance; order-structured catalyst layer

---

[*] Corresponding authors
E-mail addresses:
maochun.wu@polyu.edu.hk (M.C. Wu), zhaots@sustech.edu.cn (T.S. Zhao).

Nomenclature

List of symbols

A	Area
A_v	Specific surface area
C	Molar concentration
D	Diffusivity
F	Faraday’s constant
f_{hcb}	Packing factor of the hexagonal close pack
$f_{I/C}$	Ratio of ionomer and carbon
f_{eff}	Effective thin film thickness
H	Henry’s constant
i	Current density
i_0^{ref}	Reference exchange current density
j_a	Anode exchange current density
j_c	Cathode exchange current density
K	Permeability
k_r	Relative permeability
k_e	Evaporation rate
k_c	Condensation rate
M	Molar mass
m_{Pt}	Pt loading
m_c	Carbon loading
n_d	Electro-osmotic drag coefficient
p	Pressure
p_c	Capillary pressure
q	Heat generation rate
r	Radius
S	Source term
s	Liquid water saturation
s_c	Saturation at GDL/CH interface
s_{im}	Immobile liquid water saturation
T	Temperature

Greek symbols

α	Transfer coefficient
γ	Reaction order
δ	Thickness
ε	Porosity or volume fraction
η	Overpotential
θ_c	Contact angle
κ	Conductivity
λ	Membrane water content
μ	Dynamic viscosity
ρ	Density
τ	Tortuosity
ϕ	Potential

Subscripts

a	Anode
c	Cathode
ad	Adsorption-desorption
ec	Evaporation-condensation
eo	Electro-osmotic
CL	Catalyst layer
BL	Backing layer
MPL	Microporous layer
GDL	Gas diffusion layer
PEM	Proton exchange membrane
CH	Channel
g	Gas
ion	Ionomer
l	Liquid

Superscripts

eff	Effective value
inlet	Inlet value
ref	Reference value
ds	Disordered structure
os	Ordered structure

1. Introduction

Proton exchange membrane fuel cells (PEMFCs) are promising clean power sources for accelerating the transition toward decarbonization because of their high power density, high efficiency, and zero-emission [1–3]. Although significant advances have been achieved over the past several decades, the widespread commercialization of this technology is still hindered by several critical challenges, including high cost, insufficient power density and durability [2]. Catalyst layers (CLs), where transport of mass species, ions, and electrons simultaneously take place, are a core component that largely determines the cell performance and cost [4]. To enhance the sluggish kinetics of oxygen reduction reaction (ORR) for practical use, carbon-supported platinum (Pt)-based catalysts are usually used, which are mixed with ionomer to form CLs. Unfortunately, the random distribution and agglomerations of catalyst nanoparticles in conventional CLs not only result in poor transport pathways that limit the power output of PEMFCs, but also lead to low utilization of expensive Pt catalysts [5]. Even worse, when Pt loading is reduced in conventional CLs, PEMFCs suffer from considerable performance losses due to drastically increased oxygen transport resistances (OTRs) [6–8].

Constructing CLs with an ordered structure is conceived as an effective way to enhance mass transport and increase the utilization rate of Pt catalysts, which enables high power density with ultralow Pt loading [3,9]. In this regard, various types of ordered CLs have been developed. Debe et al. from 3M company developed nanostructured thin film (NSTF) CLs with fairly uniform ordered single crystalline whiskers by physical vapor deposition [10]. The single crystalline nature and ordered morphology of the whiskers facilitated the nucleation and growth of Pt-based catalysts, achieving superior specific activity and high utilization [10]. Tian et al. developed ordered CLs with vertically aligned carbon nanotubes (VACNT) by plasma-enhanced chemical vapor deposition. Pt catalysts were mainly dispersed on the surface of VACNT by sputtering and closely contact with the proton exchange membrane, which provided an efficient pathway for electron, proton, and oxygen transport, thereby leading to an excellent performance with ultralow Pt loading [11]. Murata et al. from Toyota company developed VACNT-based membrane electrode assemblies with a large area of 236 cm^2, which was able to deliver a high power density over 1.10 W cm^{-2} even with a low Pt loading of 0.10 mg cm^{-2}, indicating the feasibility of order-structured CLs for practical use [12]. 3D ordered hierarchical porous (3DOHP) support is another promising structure for order-structured electrodes. The stable frameworks and highly open pores of 3DOHP-based CLs can make them less susceptible to form bundle like VACNT [12–14]. Moreover, the 3DOHP structure can be directly fabricated on the gas diffusion layer substrate by self-assembly, without additional transfer process [15]. Kim et al. developed 3DOHP-based CLs with well distributed Pt catalyst by using electrodeposition on colloidal template methods. The macroscopic pores of 3DOHP-based CLs created by removing the colloidal template were interconnected and opened, which not only drastically reduced the tortuosity and improved the mass transfer, but also greatly enhance the utilization of Pt catalyst [15]. Accordingly, the PEMFC with the 3DOHP-based CLs achieved 0.84 W cm^{-2} with a low Pt loading of 0.12 mg cm^{-2}.

To provide insight into mass transport behavior in order-structured CLs, various numerical models have been developed [16]. Rao et al. [17] and Hussain et al. [18] investigated the effects of structural parameters on the performance of PEMFCs by using mathematical models, which considered the diffusion and reaction of a single unit of VACNT. It was found that the spacing of VACNT substantially affected the oxygen transport in the pores. However, these two models oversimplified mass transport processes, considering water only in vapor phase. In reality, the effect of two-phase water on mass transport processes in the ultrathin order-structured CLs is non-negligible [10]. Liang et al. developed a numerical model of VACNT-based CLs and optimized the structural parameters of VACNT by using parametric sweep. It was found that VACNT with a length of 300 nm and a space distance of 26 nm exhibited the best performance [19]. However, these existing models only simulated the microscopic units of order-structured cathode CLs, which are incapable of accurately representing the performance of the whole PEMFCs [5]. Macroscopic computational fluid dynamic models were used to describe macroscale transport behavior in the porous components and channels and predict the cell performance under various operating conditions [20–23]. However, the macroscale transport models were not suitable to describe nanoscale transport in the CLs [5]. Therefore, to accurately describe PEMFCs with order-structured CLs, a multiscale model considering both macroscopic and microscopic mass transfer is needed.

Herein, we develop a multiscale model to investigate the mass transport characteristics of ordered CLs in PEMFCs. It consists of a PEMFC macroscopic model that describes the electrochemical and mass transport process and a local oxygen transport sub-model that depicts the transfer of oxygen molecules from the bulk pores to the Pt surface. To describe the Pt-ionomer interfacial transport process accurately, a Langmuir adsorption equation is proposed in the local oxygen transport sub-model. A logarithmic normalized method is proposed to further analyze the oxygen transport characteristics. The multiscale model is validated against the experimental results using two types of order-structured CLs, i.e., 3DOHP-based and VANCT-based CLs from the literature. The effect of Pt loading, pore radius of the CLs, and relative humidity on the cell performance and local oxygen transport characteristics are systematically investigated via numerical simulations.

2. Model development

Fig. 1a illustrates the computational domain of the PEMFC macroscopic model, which is two-dimensional, two-phase, and non-isothermal. The domain contains CLs, backing layers (BLs), microporous layers (MPLs), a proton exchange membrane, ribs, and channels. The schematic of local oxygen transport processes is illustrated in Fig. 1b. Oxygen molecules need to migrate from pores in CLs to the Pt surface by going through the water film and ionomer film, which determines the effective reaction rate of oxygen reduction reaction. Fig. 1c shows the main simulation modules of the multiscale model and the coupling between the PEMFC macroscopic model and the local oxygen transport sub-model. Modules of the PEMFC macroscopic model are in the solid line, while the module of the local oxygen transport sub-model is in the dashed line. The secondary current distribution module is applied to model the electrochemical reactions, calculating potential, and current density. Water phase changes including evaporation and condensation are simulated in the two-phase water transport module, while the diffusion of gas species ($\mathrm{O_2, H_2, N_2}$) in the porous media are simulated in the gas species transport module. Water migration in the ionomer is simulated by the ionomer water transport module, which significantly affects the proton conductivity (κ_{pem}) of the ionomer. The heat transfer module is applied to consider the Arrhenius effects. To couple the PEMFC macroscopic model with the local oxygen transport sub-model, current density (i), the oxygen concentration in the bulk pores ($C_{O_2,g}$), and thickness of the ionomer and water film (δ_N, δ_w) are used as the inputs of the local oxygen transport sub-model. In return, the volumetric current density (j_c), calculated by the local oxygen transport sub-model, is integrated into the reaction equations of ORR in the secondary current distribution module.

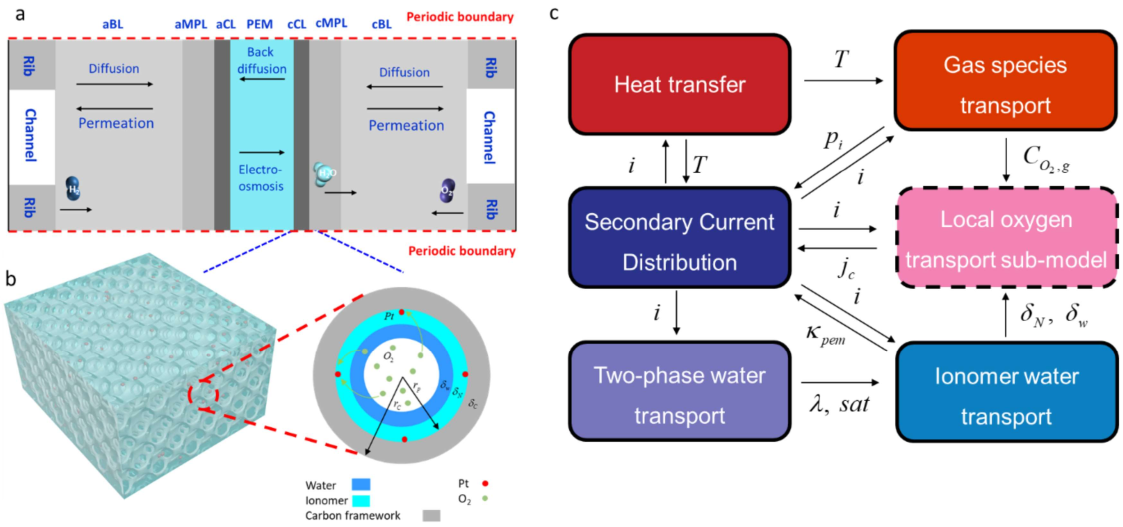

Fig. 1. Schematic of the multiscale model. (a) Computational domains of PEMFCs. (b) Representative unit of 3DOHP-based CLs in the local oxygen transport sub-model. (c) Main simulation modules and the coupling between the PEMFC macroscopic model and the local oxygen transport sub-model.

2.1. PEMFC macroscopic model

The PEMFC macroscopic model is developed based on previous models [20,24,25], where Darcy's law and Fick's law are applied to describe the fluid flow and mass transfer in the porous media. The PEMFC macroscopic model considers a steady working condition to investigate the transport of gas species and two-phase water. In this study, the following assumptions are made for the model:

1. Gas species are assumed as continuous, incompressible ideal fluids.
2. Porous electrodes, including CLs, MPLs and BLs, are assumed as homogeneous porous media.
3. Two-phase flow is assumed only in the cathode, which is laminar and incompressible. Water generation by ORR is in the gas phase.
4. Electrochemical reactions in cathode and anode are assumed as single-step reactions.
5. Active sites for oxygen reduction reaction are covered by a uniform ionomer film and water film. Water film is formed by water accumulation.
6. The membrane is impermeable to all gas species, and water transport through the membrane is driven by electro-osmosis and back diffusion.

The governing equations of the PEMFC macroscopic model consist of mass conservation, momentum conservation, energy conservation, gas species conservation, electron conservation and proton conservation. The governing equations of mass conservation, momentum conservation, and energy conservation are given by Eqs. (1) - (3), respectively.

$$\nabla(\rho\vec{u}) = S_g + S_l \tag{1}$$

where ρ, $\vec{u}$, S_g, S_l are the density of species, velocity, gas source term and liquid source term in the electrode, respectively. Source terms of each component in the governing equations are listed in Table 1.

$$\vec{u} = -K\frac{k_r}{\mu}\nabla p \tag{2}$$

where K, k_r are the absolute permeability and relative permeability, p, μ are pressure and dynamic viscosity of fluid flow in the porous media.

$$\varepsilon\rho C_p\vec{u}\nabla \mathrm{T} = \nabla\left(k^{eff}\nabla T\right) + S_T \tag{3}$$

where ε is the porosity of the porous media, T, k^{eff} are temperature and effective thermal conductivity, S_T is the energy source of joule heat, reaction heat, the heat of evaporation-condensation processes, and heat of adsorption-desorption processes.

Gas species diffusion in the porous electrodes is governed by diffusion and convection in Eq. (4),

$$\nabla(\vec{u}C_i) = \nabla\left(D_i^{eff}\nabla C_i\right) + S_i \tag{4}$$

where C_i is the concentration of gas species, D_i^{eff} is the effective diffusion coefficient, S_i is the source term of electrochemical reactions, and i denotes the gas species ($\mathrm{O_2}$, $\mathrm{H_2}$, $\mathrm{H_2O}$).

Electron conservation and proton conservation equations are given by,

$$0 = \nabla\left(\kappa_e^{eff}\nabla\phi_s\right) - j \tag{5}$$

$$0 = \nabla\left(\kappa_p^{eff}\nabla\phi_e\right) + j \tag{6}$$

where ϕ_s and ϕ_e are the potential of electrodes and electrolytes, κ_e^{eff} and κ_p^{eff} are effective electronic conductivity and effective proton conductivity.

Table 1 Source terms of the conservation equations.

Source term	Anode BL + MPL	Anode CL	PEM	Cathode CL	Cathode BL + MPL
S_i	0	S_{H_2}	0	S_{O_2}	0
S_g	0	$-S_{ad}$	$S_{eo}-S_{ad}$	$-S_{ad}-S_{ec}+S_{H_2O}$	$-S_{ec}$
S_l	0	0	0	S_{ec}	S_{ec}
S_e	0	$-j_a$	0	j_c	0
S_p	0	j_a	0	$-j_c$	0
S_T	$-j_{\mathrm{e}}\nabla\phi_{\mathrm{e}}$	$-j_e\nabla\phi_e-j_p\nabla\phi_p$ $+j_aH_{HOR}+H_{ad}S_{ad}$	$-j_p\nabla\phi_p$	$-j_e\nabla\phi_e-j_p\nabla\phi_p+j_cH_{ORR}$ $+H_{ad}S_{ad}+H_{ec}S_{ec}$	$-j_{\mathrm{e}}\nabla\phi_{\mathrm{e}}$

Given the fact that pore sizes in the CLs are mesoporous which are close to the mean free path of gas species, Knudsen diffusion is nonnegligible when Knudsen number Kn (the ratio of the molecular mean free path to the representative length of pores) is bigger than 0.01 [22]. The diffusion in the CLs should be considered as the mixture of molecular diffusion and Knudsen diffusion. Effective diffusion coefficients of gas species D_i^{eff} in catalyst layers are given by [22],

$$D_i^{eff}=\left(\frac{1}{D_{i,m}}+\frac{1}{D_{i,Kn}}\right)^{-1} \tag{7}$$

where $D_{i.m}$ and $D_{i.Kn}$ denote molecular diffusion coefficient and the Knudsen diffusion coefficient of gas species i.

Effective diffusivity is adopted to model the two-phase mass transport in the porous media, which depends on liquid water saturation and the properties of porous media [16]. The effective molar diffusivity is given by [25],

$$D_{i,m}^{eff}=\frac{\varepsilon_{\mathrm{p}}}{\tau}(1-s)^3D_i^{ref}\left(\frac{T}{T^{ref}}\right)^{1.5}\frac{p_i^{ref}}{p_i} \tag{8}$$

where s is the liquid saturation, τ is the tortuosity of porous media, ε_{p} is the porosity of the porous media, T^{ref}, D_i^{ref} and p_i^{ref} are reference temperature, reference diffusion coefficient and pressure of gas species i.

Knudsen diffusion coefficient depends on pore diameter and gas species, which is given by [20],

$$D_{i,Kn} = \frac{d_p}{3}\sqrt{\frac{8RT}{\pi M_i}} \tag{9}$$

where d_p is the diameter of pores, R is the molar gas constant, and M_i is the molar mass of gas species i.

Two-phase transport of gas and liquid water in porous media is described by Darcy's law, which depends on the permeability. The effective gas permeability of the porous media K^{eff} is given by [20],

$$K^{eff} = k_{abs}k_r \tag{10}$$

$$k_r = \begin{cases} s^3, & \text{liquid} \\ (1-s)^3, & \text{gas} \end{cases} \tag{11}$$

where k_{abs} and k_r are absolute permeability and relative permeability, respectively.

Phase change of water between liquid and vapor is described by the evaporation and condensation processes [16]. The condensation and evaporation sources (S_{ec}) are formulated as a function of reduced saturation (s_{red}) [25], given by,

$$S_{ec} = \begin{cases} \dfrac{k_e a_{lg} s_{red}(p_{H_2O} - p_{sat})}{RT} & \text{if } p_{H_2O} < p_{sat} \text{ (evaporation)} \\ \dfrac{k_c a_{lg}(1-s_{red})(p_{H_2O} - p_{sat})}{RT} & \text{if } p_{H_2O} > p_{sat} \text{ (condensation)} \end{cases} \tag{12}$$

where a_{lg} is the effective liquid-gas interfacial surface area density scaling factor, p_{H_2O} is the pressure of water, p_{sat} is the saturation pressure of water, k_e and k_c are the rates of water evaporation and condensation, respectively.

The adsorption and desorption of water vapor sources (S_{ad}) in anode and cathode CLs are defined as a function of water content (λ), which are given by [25,26],

$$S_{\mathrm{ad}} = \begin{cases} \dfrac{k_{\mathrm{a}}}{l_{CL}V_{\mathrm{m}}}\left(\lambda_{\mathrm{eq}} - \lambda\right) & \text{if } \lambda < \lambda_{\mathrm{eq}} \text{(absorption)} \\ \dfrac{k_{\mathrm{d}}}{l_{CL}V_{\mathrm{m}}}\left(\lambda_{\mathrm{eq}} - \lambda\right) & \text{if } \lambda > \lambda_{\mathrm{eq}} \text{(desorption)} \end{cases} \tag{13}$$

$$\lambda = \left(1 + 7.75 \times 10 - 3a^2(T - 303.15)\right)\left(14.22a^3 - 18.9a^2 + 13.4a\right) \tag{14}$$

where λ_{eq} is the equilibrium water content of the ionomer, a is water activity, k_{a} and k_{d} are the rates of water adsorption and desorption in the CLs. l_{CL} is the thickness of CLs. V_{m} is the molar volume of the ionomer. The expression of water activity (a), equilibrium water content of the ionomer (λ_{eq}) and related physical properties in the PEMFC macroscopic model are given in Table 2.

Water transport across the proton exchange membrane is mainly determined by back diffusion and electro-osmosis, which is described by [16],

$$N_w = n_d \frac{i}{F} - \frac{k_{pem}\rho_l \Delta p}{M_{H_2O}\mu_l l_{PEM}} \tag{15}$$

$$n_d = \begin{cases} 0, & 0 < \lambda < 5 \\ 1, & 5 \le \lambda < 14 \\ 2.5, & \lambda \ge 14 \end{cases} \tag{16}$$

where n_d is electro-osmotic drag coefficient of water, $M_{\mathrm{H_2O}}$ is molar mass of water, l_{PEM} is the thickness of PEM. k_{pem} is the water permeability of membrane, and μ_l is the viscosity of water in membrane.

Table 2 Physical properties.

Parameters	Expression	Ref.
Arrhenius expression	$k_a = \exp\left(\dfrac{E}{R}\dfrac{1}{1/353.15 - 1/T}\right)$	[25]
Water activity	$a = 2s + C_{\mathrm{H_2O}}RT / p_{\mathrm{sat}}$	[21]
Water saturation pressure [Pa]	$p_{sat} = exp(23.1963 - \dfrac{3816.44}{T - 46.13})$	[27]
Capillary pressure [Pa]	$p_{\mathrm{c}} = p_{\mathrm{g}} - p_{\mathrm{l}} = \sigma \cos\theta_{\mathrm{c}} (\varepsilon / K)^{0.5} J(s)$ $J(s) = \begin{cases} 1.417(1-s) - 2.120(1-s)^2 + 1.263(1-s)^3 & 0 < \theta_c < 90^{\circ} \\ 1.417s - 2.120s^2 + 1.263s^3 & 90^{\circ} < \theta_{\mathrm{c}} < 180^{\circ} \end{cases}$	[27]

Equilibrium water content of the ionomer	$\lambda_{\mathrm{eq}} = \begin{cases} 0.043 + 17.81a - 39.85a^2 + 36.0a^3 & 0 \le a \le 1 \\ 14.0 + 1.4(a - 1.0) & 1 < a \le 3 \end{cases}$	[21]
Volume fraction of water in membrane	$f = \frac{\lambda V_{\mathrm{w}}}{\lambda V_{\mathrm{w}} + V_{\mathrm{m}}}$	[25]
Proton conductivity of membrane $[\mathrm{S\ m^{-1}}]$	$\kappa_{\mathrm{p}} = 116\varepsilon_p^{1.5}(\frac{\lambda V_{\mathrm{w}}}{\lambda V_{\mathrm{w}} + V_{\mathrm{m}}} - 0.06)^{1.5} k_a$	[25]
Viscosity of liquid water $[\mathrm{m\ Pa\ s}]$	$\mu = \exp(-3.63148 + \frac{542.05}{T - 144.15})$	[25]
Water diffusivity in the ionomer $[\mathrm{m^2\ s^{-1}}]$	$D_\lambda = \varepsilon_p \frac{3.842\lambda^3 - 32.03\lambda^2 + 67.74\lambda}{\lambda^3 - 2.115\lambda^2 - 33.013\lambda + 103.37} \times 10^{-10}$	[25]

The modified Butler-Volmer equation with Pt-oxide-coverage-dependent kinetics Eq. (17) [28] is used to describe ORR in the cathode CLs, where θ_{PtO} is the oxide coverage, which is a function of potential given by Eq. (18), ω is the coverage-dependent rate of adsorption, and the reaction order of ORR (γ_c) in the cathode is set as 0.7 [28].

$$j_c = A_c i_{0,c}^{ref}\left(1 - \theta_{\mathrm{PtO}}\right)\left(\frac{C_{O_2,Pt}}{C_{0,ORR}^{ref}}\right)^{\gamma_c} \exp\left(-\frac{\alpha_c}{RT}F\eta_{\mathrm{c}} - \frac{\omega\theta_{\mathrm{PtO}}}{RT}\right) \tag{17}$$

$$\theta_{\mathrm{PtO}} = 1/\left(1 + \mathrm{e}^{22.4(0.818 - E)}\right) \tag{18}$$

where η_{c} is cathode overpotential, $C_{0,ORR}^{ref}$ is the reference exchange current density for ORR, and α_c is the transfer coefficient of ORR.

For calculation of hydrogen oxidation reaction (HOR) rate in the anode CLs, a simplified Butler-Volmer equation was given,

$$j_a = A_a i_{0,\mathrm{a}}^{ref}\left(\frac{C_{H_2,a}}{C_{0,HOR}^{ref}}\right)^{\gamma_a} \exp\left(\frac{\alpha_a}{RT}F\eta_a\right) \tag{19}$$

where η_a is anode overpotential, $C_{0,HOR}^{ref}$ is the reference exchange current density for HOR, and α_a is the transfer coefficient of HOR.

The active specific surface area (A_c, A_a) of cathode and anode CLs could be expressed by Pt loading,

$$A_c = \frac{E_c}{\delta_{cCL}} = \frac{3m_{Pt.c}}{\rho_{Pt} r_{Pt} \delta_{cCL}} \tag{20}$$

$$A_a = \frac{E_a}{\delta_{aCL}} = \frac{3m_{Pt.a}}{\rho_{Pt} r_{Pt} \delta_{aCL}} \tag{21}$$

where $m_{Pt,c}$, $m_{Pt,a}$ is the Pt loading of cathode and anode CLs, ρ_{Pt}, r_{Pt} is the density and particle radius of Pt catalyst, and δ_{cCL}, δ_{aCL} is the thickness of cathode and anode CLs. Geometric parameters, physicochemical properties, and operation conditions of the PEMFC are listed in Table 3.

Table 3 Parameters of the PEMFC macroscopic model.

Parameters	Expression	Value	Unit	Ref.
Layer thickness	δ_{GDL}, δ_{MPL}, δ_{CL}, δ_{PEM}	160, 30, 5, 25	μm	[20]
Tortuosity	τ_{cCL}^{os}, τ_{cCL}^{ds}, τ_{GDL}, τ_{MPL}	1.2, 2.0, 3.0, 3.0		[20]
Porosity	ε_{GDL}, ε_{MPL}, ε_{aCL}	0.7, 0.3, 0.3		[20]
Permeability	K_{GDL}, K_{MPL}, K_{CL}, K_{PEM}	2×10^{-12}, 2×10^{-12}, 1×10^{-14}, 2×10^{-18}	m^2	[22]
Diffusivity	$D_{O_2,ref}$, $D_{H_2,ref}$, $D_{H_2O,ref}$	2.8×10^{-5}, 1.24×10^{-4}, 3.6×10^{-5}	m^2s^{-1}	[25]
Viscosity	μ_g, μ_l	2.03×10^{-5}, 4.06×10^{-4}	$kg\ m^{-1}s^{-1}$	[27]
Evaporation rate constant	k_e	5×10^{-3}	$atm^{-1}\ s^{-1}$	[25]
Condensation rate constant	k_c	5×10^{-5}	atm^{-1} mol	[25]
Saturation at interface	s_c	0.12		[25]
Inlet pressure	p_{inlet}	1.5	atm	[15]
Temperature	T_{cc}	353.15	K	[15]
Relative humidity	RH	100%		[15]

2.2. Local oxygen transport sub-model

The local oxygen transport sub-model is developed to describe the mass transfer of oxygen molecules from bulk pores to the Pt surface. The transport processes consist of the following five steps as shown in Fig. S1. (1) Oxygen interfacial dissolution process from bulk pores to the water film, (2) Oxygen diffusion process in the water film, (3) Oxygen interfacial dissolution process from water to ionomer, (4) Oxygen diffusion process in the ionomer film, and (5) Oxygen interfacial adsorption process from ionomer to Pt surface.

Oxygen interfacial dissolution from bulk pores into water film can be determined by Henry's law,

$$C_{O_2,1} = C_{O_2,g} \frac{RT}{H_{O_2,w}} \tag{22}$$

where $C_{O_2,1}$ is the oxygen concentration resulting from the interfacial dissolution process, and $H_{O_2,w}$ is the Henry's constant of oxygen in the water film, which is given in Table 4.

The oxygen diffusion in the thin water film can be given by,

$$N_{O_2} = (C_{O_2,2} - C_{O_2,1}) \frac{D_{O_2,w}}{\delta_w} \tag{23}$$

where $C_{O_2,2}$ is the oxygen concentration resulting from oxygen diffusion in the thin water film, $D_{O_2,w}$ is the diffusion coefficient of oxygen in the water film. δ_w is the thickness of the water film accumulated and N_{O_2} is the oxygen flux of the local oxygen transport processes.

Oxygen interfacial dissolution from water into ionomer could be characterized as the dissolution step and the interfacial step. The dissolution step from water to ionomer phase can be obtained by Henry's law and the interfacial step from water to ionomer phase can be expressed as proportional to the ionomer diffusive resistance [29].

$$C_{O_2,w-ion} = C_{O_2,2} \frac{H_{O_2,ion}}{H_{O_2,w}} \tag{24}$$

$$N_{O_2} = (C_{O_2,3} - C_{O_2,w-ion}) k_{w-ion} \tag{25}$$

$$\frac{1}{k_{w-ion}} = \frac{1}{3} \frac{\delta_{ion}}{D_{O_2,ion}} \tag{26}$$

where $C_{O_2,3}$, $C_{O_2,w\text{-}ion}$ are oxygen concentrations resulting from the dissolution and interfacial steps, $H_{O_2,ion}$, $H_{O_2,\mathrm{w}}$ are Henry's constant of oxygen in ionomer and water, $D_{O_2,\mathrm{ion}}$ is the diffusion coefficient of oxygen in the ionomer, δ_{ion} is the thickness of the ionomer film, and k_{w-ion} is the water-ionomer interfacial resistance.

The oxygen diffusion process in the ionomer film can be given by,

$$N_{O_2} = (C_{O_2,4} - C_{O_2,3}) \frac{D_{O_2,ion}}{\delta_{ion}} \tag{27}$$

where $C_{O_2,4}$ is oxygen concentration resulting from oxygen diffusion process in the ionomer film.

The Pt-ionomer resistance was simplified as a fixed value or proportional to the bulk resistance in previous works [7,22,24], which underestimated the ionomer-Pt resistance severely. Even worse, these simplifications contradict the molecular dynamic investigation results [30,31]. Although the adsorption mechanism of oxygen reactant on Pt active sites is still debatable, Langmuir adsorption can fit well with the adsorption process [32–34]. Thus, Langmuir adsorption equations can be applied to describe the oxygen adsorption on Pt surface to investigate interfacial resistances, which can be described as,

$$C_{O_2,Pt} = C_{O_2,max} \frac{K_L C_{O_2,4}}{1 + K_L C_{O_2,4}} \tag{28}$$

where maximum oxygen concentration $C_{O_2,max}$ on Pt surface could be calculated by,

$$C_{O_2,max} = \frac{\theta_{max}}{N_A} A_{Pt} \rho_{O_2} \tag{29}$$

where θ_{max} is the maximum oxygen adsorption coverage on Pt surface, N_A is the Avogadro constant, and A_{Pt} is the electrochemical specific surface area of Pt. The maximum oxygen adsorption coverage on the Pt surface is estimated by Kelvin probe measurement and density function theory calculation [35]. Parameters of the local oxygen transport sub-model are listed in Table 4.

Table 4 Parameters of the local oxygen transport sub-model.

Parameters	Expression	Value	Unit	Ref.
Diffusion coefficient	$D_{O_2,w}$, $D_{O_2,ion}$	2.2×10^{-9}, 1.8×10^{-10}	m^2 s^{-1}	[22]
Henry's constant	$H_{O_2,w}$, $H_{O_2,ion}$	1.26×10^{5}, 2.04×10^{5}	Pa m^3 mol^{-1}	[36]
Reference exchange current density	$i_{0,HOR}^{ref}$	2.15×10^{-2}	A cm^{-2}	[24]
	$i_{0,ORR}^{ref}$	3×10^{-5}	A cm^{-2}	Fitted [24]
Reference concentration	$C_{0,HOR}^{ref}$	4×10^{-5}	mol m^{-3}	[20]
	$C_{0,ORR}^{ref}$	2.4×10^{-3}	mol m^{-3}	Fitted
Langmuir adsorption coefficient	K_L	0.2		Fitted
Transfer coefficient	α_a, α_c	0.5, 0.5		[24]

Concentration coefficient	γ_a, γ_c	1, 0.7		[24]
Max oxygen adsorption	θ_{max}	4.2×10^{19}	atoms/m^2	Fitted [35]

Oxygen flux in the local oxygen transport model can be given by Faraday's law,

$$N_{O_2} = \frac{j_c}{4Fa_{ion}} \tag{30}$$

where a_{ion} is the volumetric surface area of the active site in the ionomer.

In addition, the highly dispersed Pt particles exist only in a few sites on the carbon support when Pt loading is ultralow [8,24]. Oxygen molecules far away from the Pt particles need to go through a much longer diffusion length than those near the Pt particles. As a result, the diffusion length in the ionomer should be revised by the effective coefficient of diffusion length f_{dif}^{eff}, which can be defined as a function of the effective surface area ratio, given by Eqs. (31) - (33),

$$A_{ion}^{eff} = 4\pi\left(r_p - \delta_{ion}\right)^2 \tag{31}$$

$$A_{Pt}^{eff} = 4\pi r_{Pt}^2\left(1-\theta_{\text{PtO}}\right)\frac{m_{Pt}}{L_{cCL}}\frac{(r_p+\delta_c)^3}{\rho_{Pt}{r_{Pt}}^3} \tag{32}$$

$$f_{dif}^{eff} = (\sec(\arctan(\frac{A_{ion}^{eff}}{A_{Pt}^{eff}}))+1)/2 \tag{33}$$

To solve transport equations of the local oxygen transport sub-model, the geometric parameters of the representative units are needed. Since PEMFCs are applied in high power densities, the water accumulation is non-negligible. Pt volume fraction is neglected due to ultralow Pt loading. The volume fractions are governed by Eq. (34),

$$\varepsilon_C + \varepsilon_p + \varepsilon_{ion} + \varepsilon_w = 1 \tag{34}$$

where ε_C, ε_p, ε_{ion}, and ε_w are the volume fraction of carbon support, pores, ionomer film, and water film.

And the geometry derivation of 3DOHP can be given by Eqs. (35) - (40), while the geometry derivation of VACNT-based CLs is given in supporting information. In the representing unit of 3DOHP catalyst layers, Pt catalysts are deposited on the surface of sphere carbon support and covered by the ionomer thin film and water thin film, as depicted in Fig. S1. The voids of 3DOHP catalyst layers are created by removing the polystyrene spheres (PS) templates with hexagonal-close-packing. Thus, carbon support takes up the remaining space. The volume fraction of carbon support is given by,

$$\varepsilon_C = 1 - f_{hcp} \tag{35}$$

where f_{hcp} is the packing coefficient of the hexagonal-close-packing.

For simplicity of calculating the volumetric properties of the 3DOHP catalyst layer, the unit of 3DHOP catalyst layers in a sphere shape is given as fig. S1. The thickness of carbon support (δ_C) in the sphere unit is given by,

$$\delta_C = (f_{hcp}{}^{-1/3} - 1) r_p \tag{36}$$

where r_p is the radius of pores of 3DOHP-based CLs.

As the volume of the ionomer expands with water uptake, the volume fraction of the ionomer film (ε_{ion}) should be revised by the expansion factor in wet conditions by Eq. (37) [24], and the corresponding thickness of ionomer (δ_{ion}) in the sphere unit is given by Eq. (38),

$$\varepsilon_{ion} = f_{I/C} \varepsilon_C \frac{\rho_c}{\rho_e} \left(1 + \frac{M_w \rho_e}{\rho_w EW} \lambda \right) \tag{37}$$

$$\delta_{ion} = r_P - \left[r_P{}^3 - (r_P + \delta_C)^3 \varepsilon_{ion} \right]^{1/3} \tag{38}$$

where $f_{I/C}$ is the ratio of ionomer and carbon, M_w is the molar weight of ionomer, ρ_e is the density of ionomer electrolyte, ρ_c is the density of carbon support, ρ_w is the density of liquid water, EW is the equivalent weight of ionomer.

The water film is related to the liquid water accumulation [22], and the thickness of water film (δ_w) is given by,

$$\delta_w = r_P - \delta_{ion} - \left[(r_P - \delta_{ion})^3 - \frac{3s}{4\pi} (r_P + \delta_C)^3 \right]^{1/3} \tag{39}$$

where s is the liquid water saturation.

The volumetric surface area of the active site in the ionomer (a_{ion}) is given by [24],

$$a_{ion} = \frac{3\varepsilon_C (r_p - \delta_{ion})^2}{r_C^{\ 3}} \tag{40}$$

2.3. Boundary conditions

The governing equations with source terms in Table 1 are solved subjected to the following boundary conditions.

For the boundary in the cathode gas diffusion layers under channels and ribs,

Channel: $$C_{O_2} = C_{O_2,in},\ p_{O_2} = p_{O_2,in},\ p_{H_2O} = p_{H_2O,in},\ T_c = T_{cc} \tag{35}$$

Rib: $$\frac{\partial C_{O_2}}{\partial y} = 0,\ \frac{\partial p_{O_2}}{\partial y} = 0,\ \frac{\partial p_{H_2O}}{\partial y} = 0,\ T_c = T_{cc}, \phi_s = E_{cell} \tag{36}$$

For the boundary in the anode gas diffusion layers under channels and ribs,

Channel: $$C_{H_2} = C_{H_2,in},\ p_{H_2} = p_{H_2,in},\ p_{H_2O} = p_{H_2O,in},\ T_a = T_{cc} \tag{37}$$

Rib: $$\frac{\partial C_{H_2}}{\partial y} = 0,\ \frac{\partial p_{H_2}}{\partial y} = 0,\ \frac{\partial p_{H_2O}}{\partial y} = 0,\ T_a = T_{cc},\ \phi_s = 0 \tag{38}$$

For the boundary in the periodic boundary,

$$\frac{\partial C_i}{\partial n} = 0,\ \frac{\partial p_i}{\partial n} = 0,\ \frac{\partial \phi_s}{\partial n} = 0,\ \frac{\partial \phi_l}{\partial n} = 0 \tag{39}$$

2.4. Numerical implementation

The above governing equations, source items, and physical correlations from the PEMFC macroscopic model and the local oxygen transport sub-model were solved by COMSOL Multiphysics(R) 5.6 with stationary solvers. Simulations were completed with the workstation with 12 processors (Intel Xeon(R) W-2275 CPU @ 3.30GHz). The mesh was created by sweep mesh, with mesh refinement of CLs and membrane. Mesh independence test was conducted to ensure the accuracy of the numerical results. The relative tolerance was set to 1 × 10^{-6}. Parametric sweeps of cell voltage were conducted to obtain the polarization performance of PEMFCs.

3. Oxygen transport resistance analysis method

The total OTR is defined as the ratio of the oxygen concentration difference and oxygen flux of the whole transport processes [6],

$$R_{total} = \frac{C_{O_2,CH} - C_{O_2,Pt}}{N_{O_2}} = \frac{4F(C_{O_2,CH} - C_{O_2,Pt})}{i} \tag{46}$$

where $C_{O_2,CH}$ is the oxygen concentration in channels, N_{O_2} is the oxygen flux, and i is the current density.

In the limiting current measurement, $C_{O_2,Pt}$ can be considered as 0 [6,7]. Thus, total OTR defined by the conventional limiting current method can be calculated by,

$$R_{total,lim} = \frac{4FC_{O_2,CH}}{i_{lim}} \tag{47}$$

where i_{lim} is the limiting current density.

For quantitative analysis of OTRs, total OTR is divided into bulk OTRs resulting from diffusion in porous media (BL, MPL, CL) and local OTRs corresponding to the transport processes from bulk pores to Pt surface in CL. The bulk OTR can be given by,

$$R_{i,bulk} = \frac{1}{N_{O_2}} \int_i \frac{dC_{O_2,i}}{dx},\ i = BL, MPL, CL \tag{48}$$

And the local OTR can be given by,

$$R_{CL,local} = \frac{4FC_{O_2,CH}}{i_{lim}} - R_{CL,bulk} - R_{MPL,bulk} - R_{BL,bulk} \tag{49}$$

OTRs can be measured by using the limiting current method [6,7]. However, under the non-limiting current conditions, Eq. (47) cannot be used to describe the total OTR, because $C_{O_2,Pt}$ is several orders of magnitude smaller than $C_{O_2,\mathrm{CH}}$. When the operating voltage is increased to the non-limiting current conditions, the numerator (oxygen concentration) of Eq. (47) stays almost unchanged, as the local oxygen concentration is negligible to the bulk oxygen concentration, but the denominator (current density) is reduced. It would lead to the increase of the results of local OTR, contrary to the experimental phenomenon that the local OTRs are smaller under the non-limiting conditions than that under the limiting conditions. Thus, using the conventional method (Eq. (47)) is inappropriate under the non-limiting current conditions.

The logarithmic normalized method is proposed to calculate local OTRs under the limiting and non-limiting current conditions, as the effect of local oxygen concentration on the volumetric current density in Eq. (17) is logarithmic. This method defines logarithmic normalized oxygen concentration (c_i) and logarithmic normalized oxygen transport resistance (r_i) by Eqs. (50) - (51).

$$c_i = \log(\frac{C_{O_2,i}}{C_{O_2,ref}}) \tag{50}$$

$$r_i = c_i - c_{i+1} = \log(\frac{C_{O_2,i}}{C_{O_2,i+1}}) \tag{51}$$

The total logarithmic normalized OTR can be divided by resistances from the interfacial processes and diffusive processes by Eq. (52), including gas-water interfacial resistance ($r_{g-w,\text{int}}$), water diffusive resistance ($r_{w,dif}$), water-ionomer interfacial resistance ($r_{w-ion,\text{int}}$), ionomer diffusive resistance ($r_{ion,dif}$), and ionomer-Pt interfacial resistance ($r_{ion-Pt,\text{int}}$). By using this method, the impacts of the five local transport processes can be quantified and compared directly, allowing us to find the rate-determine step of the local oxygen transport processes.

$$r_{total,local} = r_{g-w,\text{int}} + r_{w,dif} + r_{w-ion,\text{int}} + r_{ion,dif} + r_{ion-Pt,\text{int}} \tag{52}$$

4. Results and discussion

4.1. Validation

The multiscale model was first validated against the experimental data from the previous works that used 3DOHP-based CLs [15]. As shown in Fig. 2, the simulated polarization curves are in good agreement with the experimental results of PEMFC using the 3DOHP-based CLs [15]. It is found that PEMFC with conventional and ordered CLs exhibits almost the same activation polarization and similar ohmic polarization. However, the PEMFC with conventional CLs suffers from severe concentration polarization. In contrast, the 3DOHP-based CLs enable the PEMFC to achieve a much higher limiting current density thanks to the significantly enhanced mass transport enabled by the ordered structure with low tortuosity. In addition, by using geometrical and physical properties of VACNT-based CLs [19], the as-developed model can well simulate the electrochemical performance of PEMFC with the VACNT-based CLs (Fig. S2), demonstrating the excellent capability of our model in simulating the PEMFC with different types of ordered CLs. As the 3DOPH-based CLs have advantages in easy fabrication and less susceptibility of forming bundles [12–14], 3DOPH-based CLs were chosen as an example in this work to systematically investigate the mass transport characteristics.

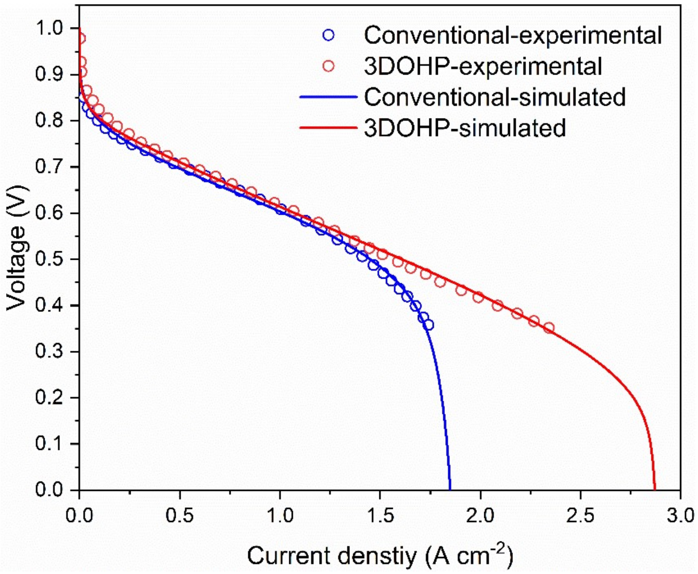

Fig. 2. Validation of the multiscale model against the experimental results of 3DOHP-based CLs [15].

4.2. Effect of Pt loading

As the loading of Pt catalyst plays a critical role in determining the performance of PEMFCs, the influence of Pt loading on cell performance is first investigated. As shown in Fig. 3, when Pt loading is reduced, not only the activation polarization but also the concentration polarization is significantly increased. The increase of activation loss can be ascribed to the reduced electrochemical specific surface, while the increased concentration polarization is mainly due to the increased local OTR, because the local oxygen diffusion length is much larger at lower Pt loading. It is also found that the decrease in limiting current density is more pronounced at ultralow Pt loading. As can be seen, when the Pt loading is reduced from 0.20 to 0.04 mg cm^{-2}, the limiting current density declines from 3.05 to 2.18 A cm^{-2}, but it drops significantly to as low as 1.03 A cm^{-2} when the loading further is reduced to 0.01 mg cm^{-2}. The results indicate the dramatic increase of concentration polarization loss when the Pt loading is significantly reduced.

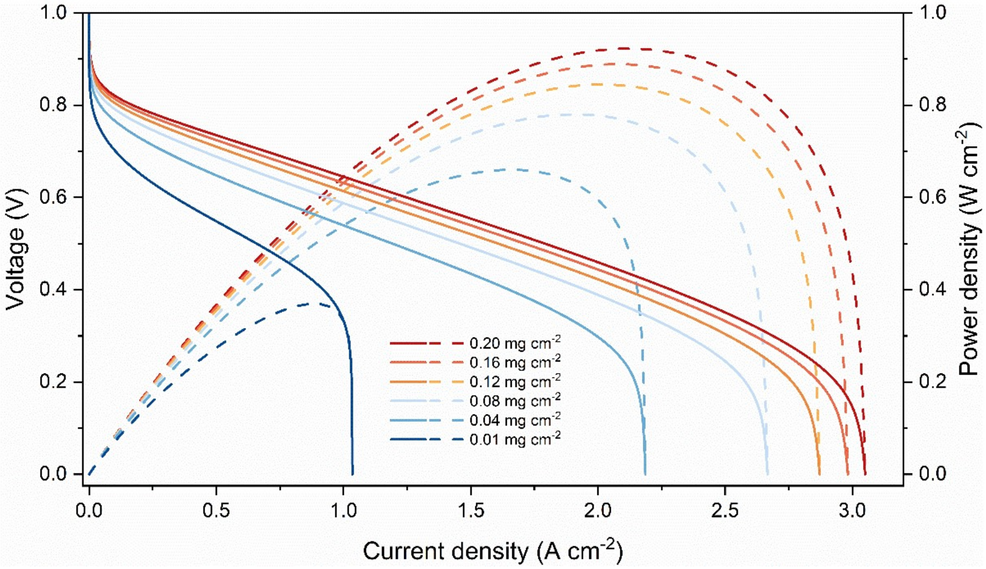

Fig. 3. PEMFC performance with different Pt loading.

To better understand the origin of concentration polarization, OTRs are calculated under the limiting current condition. As depicted in Fig. 4, with the reduction of Pt loading, the total OTR increases significantly. In particular, the local OTR from CL ($R_{CL,local}$) increases remarkably, while bulk OTRs from BL, MPL, and CL ($R_{BL,bulk}$, $R_{MPL,bulk}$, $R_{\mathrm{CL},bulk}$) change not much. This can be explained as follows. Bulk OTRs come from diffusion resistance in porous media, which are proportional to the thickness of the porous media and inversely correlated to the effective diffusion coefficient and liquid water saturation [22]. When varying Pt loading, the saturation in porous media change not significantly (as shown in Fig. S4 in the supporting information), resulting in small changes of bulk OTRs. In contrast, reducing Pt loading leads to increased diffusion length in ionomer, resulting in much larger local diffusive resistance according to Eqs. (31) - (33). Meanwhile, reducing Pt loading contributes to a smaller $C_{O_2,max}$ in the Langmuir adsorption equations, causing a larger ionomer-Pt interfacial resistance. Both the increased resistances of the local diffusive and interfacial transport processes lead to the drastic increase of $R_{CL,local}$.

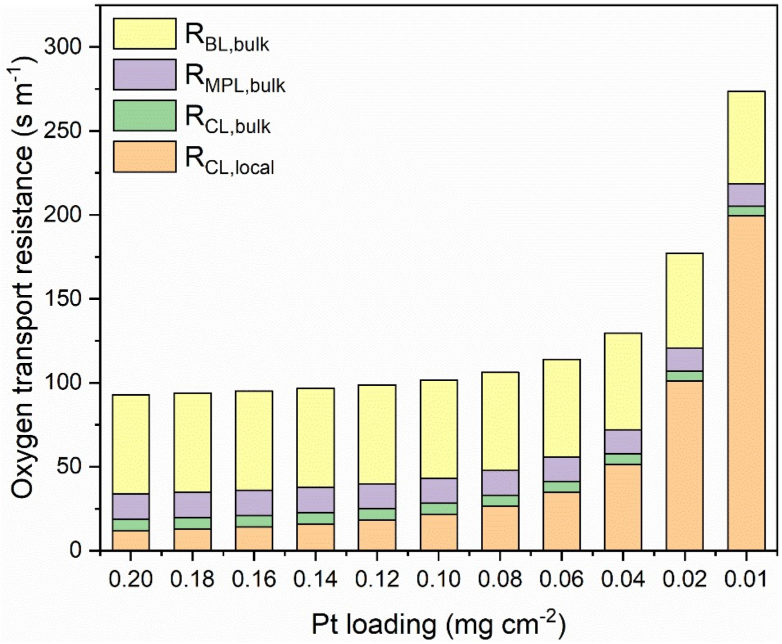

Fig. 4. Oxygen transport resistance with different Pt loading.

The relationship between local OTRs from CLs and Pt loading is further analyzed by correlating the local OTRs with Pt loading as well as roughness factor. The roughness factor (the ratio of electrochemical specific surface area and membrane electrode assembly area) is a dimensionless parameter commonly used to describe the effect of Pt loading on the non-Fickian oxygen transport [1,6,37]. As shown in Fig. 5, when Pt loading is higher than 0.10 mg cm^{-2}, the local OTRs are relatively insensitive to the Pt loading. However, the local OTRs increase dramatically with the reduction of Pt loading when Pt loading is smaller than 0.10 mg cm^{-2}. Specifically, when Pt loading is reduced to 0.01 mg cm^{-2}, the local OTR approaches as high as 200 s m^{-1}, which is 10 times larger than that of 0.10 mg cm^{-2} Pt loading, hindering the cell performance. Since the effective coefficient of diffusion length (f_{dif}^{eff}) is negatively correlated with Pt loading, ultralow Pt loading results in significantly increased diffusion resistances in ionomer. Moreover, as indicated by Eq. (29), ultralow Pt loading leads to much weaker adsorption and thus larger interfacial resistance. Overall, the local OTRs exhibit a linear relationship with the reciprocal of roughness factor as shown in the inset of Fig. 5, which is consistent with experimental results [37] and theoretical derivation [6], confirming the rationality of the local oxygen transport sub-model in section 2.2. The slope of the linear function (OTR of such order-structured CLs) is 692.33 s m^{-1}, which is about 63% smaller than that of the conventional CLs calculated by our models, demonstrating the superior local oxygen transport properties of order-structured CLs.

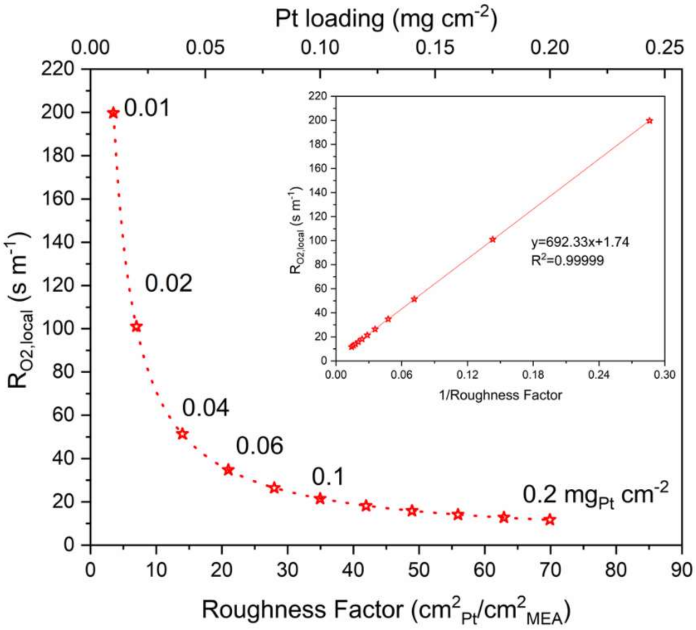

Fig. 5. Local oxygen transport resistance with different roughness factors and Pt loading. The inset shows the curve fitting of the reciprocal of roughness factor and the local oxygen transport resistance.

By using the proposed logarithmic normalized method for OTRs, the oxygen transport characteristics of order-structured and conventional CLs are compared in Fig. 6. It is noted that PEMFCs with ordered CLs exhibit larger current density than the conventional CLs with the same voltage (see Fig. 3), which is due to the larger local oxygen concentrations ($C_{O_2,Pt}$) of the order-structured CLs. Under the limiting current conditions (voltage approaches zero), the profiles of the local oxygen concentrations are shown in Fig. 6b, in the form of logarithmic normalized concentrations. It can be seen that the local oxygen concentrations of order-structured CLs are higher than those of conventional CLs. In contrast, the bulk oxygen concentration of the conventional CLs is larger than that of the order-structured CLs in Fig. 6a. The discrepancy of bulk and local oxygen concentrations comes from the fact that the local OTRs of order-structured CLs are much smaller than that of the conventional CLs, shown in Fig. 6c. In both the conventional and order-structured CLs, the local OTRs increase with the decreased Pt loading, while the former suffers from a more significant increase of local OTR at low Pt loading. The local OTRs of conventional CLs are more than 2.5 times larger than that of order-structured CLs with 0.01 mg cm^{-2} Pt loading. This can be ascribed to the fewer Pt active sites and smaller electrochemical specific area in the conventional CLs than in order-structured CLs with the same Pt loading, since Pt particles on the mesoporous carbon support in the conventional CLs are easier to aggregate and more inaccessible. The smaller electrochemical specific area causes a bigger f_{dif}^{eff} according to Eq. (33), resulting in higher local OTRs of conventional CLs.

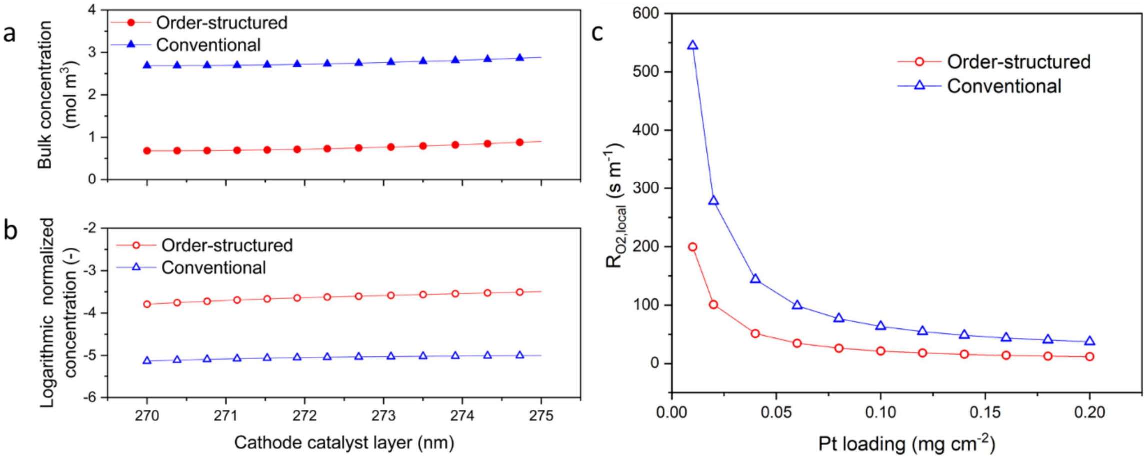

Fig. 6. Comparison between order-structured and conventional CLs. (a) Bulk and (b) Local oxygen concentration profiles in the cathode CLs with Pt loading of 0.12 mg cm^{-2}. (c) Local oxygen transport resistance with different Pt loading.

To gain a better understanding of local oxygen transport characteristics, oxygen concentrations and the local logarithmic normalized OTRs in CLs are depicted and compared in Fig. 7. In CLs, oxygen from pores undergoes the abovementioned five oxygen transport processes to Pt surface (described in section 2.2 and Fig. S1), as depicted by the black arrow from the curve of $C_{O_2,g}$ to the curve of $C_{O_2,Pt}$ in Fig. 7a. It should be noted that the curves of $C_{O_2,1}$ and $C_{O_2,2}$ overlap in Fig. 7a, due to a small diffusive resistance in water film (almost zero) as calculated in Fig. 7b. It can be seen that $C_{O_2,g}$ and $C_{O_2,Pt}$ show opposite trends (the increase of $C_{O_2,g}$ and decrease of $C_{O_2,Pt}$) with decreased Pt loading. When Pt loading is less than 0.04 mg cm^{-2}, the opposite trend of two curves is more significant, indicating the dramatical increased resistance of oxygen interfacial adsorption process from ionomer to Pt surface. The increase of $C_{O_2,g}$ is ascribed to the reduction of oxygen consumption of ORR with reducing Pt loading, while the decrease of $C_{O_2,Pt}$ is ascribed to the increased local OTRs of oxygen transport processes. Fig. 7b shows the impacts of local oxygen transport processes. It can be observed that with the reduction of Pt loading, the $r_{ion-Pt,int}$ increases remarkably, while the other resistances keep almost unchanged. The increase of $r_{ion-Pt,int}$ can be ascribed to weaker adsorption on the ionomer-Pt interface, since reducing Pt loading leads to smaller $C_{O_2,max}$ in Langmuir adsorption equations according to Eq. (28) and (29).

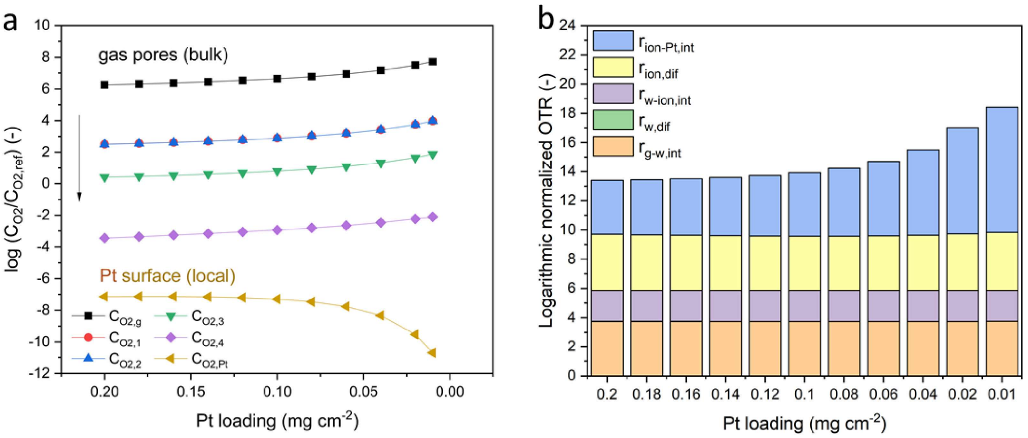

Fig. 7. Local oxygen transport resistances under the limiting current conditions. (a) Logarithmic oxygen concentration and (b) Logarithmic normalized oxygen transport resistances.

To investigate local oxygen transport processes under the non-limiting current conditions, local OTRs at voltages from 0.45 to 0 V are investigated. It is noted that 0.45 V is selected because this voltage approaches the operating voltage to achieve peak power density (as shown in Fig. 3). Fig. 8 shows the effect of Pt loading and operating voltage on logarithmic normalized OTRs in a 3D spatial plot. When operating at a relatively high voltage, the oxygen consumption is relatively small and the remaining oxygen concentration is relatively high, resulting in very low logarithmic normalized OTRs. As the operating voltage decreases, the current density is increased, corresponding to a higher oxygen consumption that would lead to a lower remaining oxygen concentration. Due to the Langmuir adsorption, lower local oxygen concentrations would cause much higher $r_{ion-Pt,\text{int}}$. As a result, when the voltage decreases less than 0.45 V, the increase of logarithmic normalized OTR is significant, as illustrated in Fig. 8. The most significant increase of logarithmic normalized local OTRs is observed when Pt loading is less than 0.04 mg cm^{-2} and the operating voltage is less than 0.45 V. Besides, to investigate the impact of local oxygen transport process under the non-limiting conditions, local OTRs are compared in Fig. S3. It is found that the increase of ionomer diffusive resistance ($r_{ion,dif}$) is obvious in Fig. S3b and d, because of the fast drop of $C_{O_2,4}$ in Fig. S3a and c. Since both the Pt loading and operating voltage affect the local oxygen transport, a balance of the two parameters is needed to achieve the peak power density of PEMFCs.

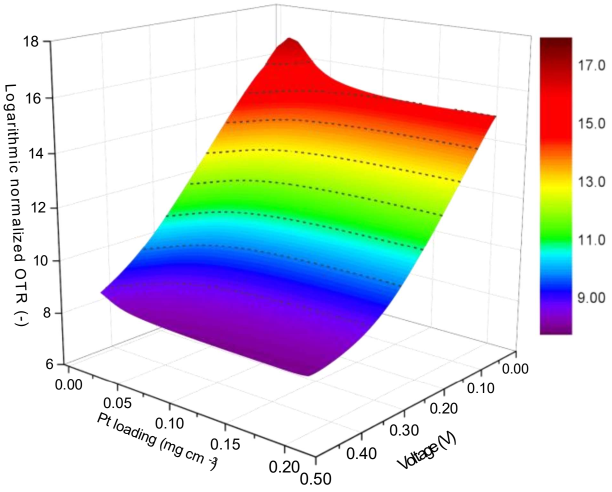

Fig. 8. Effect of Pt loading and operating voltage on the logarithmic normalized oxygen transport resistance.

4.3. Effect of pore size

Pore size of order-structured CLs is a key parameter that affects the performance of PEMFCs. Fig. 9a displays the polarization curves of PEMFCs with various pore radii of CLs. It is revealed that larger pores in CLs show better mass transport properties but suffers from higher activation polarization. This is understandable because increasing the radius of pores can result in the increased bulk diffusion coefficient but sacrifice the volumetric specific area of 3DOHP support in the representative unit, which leads to a larger activation loss. It is indicated that the order-structured CLs with a radius of 150 nm enables the PEMFC to achieve the highest peak power density of 0.90 W cm^{-2} and the highest limiting current density of 2.26 A cm^{-2}. Oxygen transport resistance analysis by the conventional limiting current method and the proposed logarithmic OTR method are presented in Fig. 9b. It can be found that increasing pore radius can reduce both OTRs calculated by limiting current method and logarithmic normalized method. Although OTRs calculated by two methods show similar tendencies, the proposed logarithmic normalized method can reveal the nature of local oxygen transport by calculating the change of local oxygen concentrations directly. In contrast, OTRs calculated by the limiting current method are only influenced by the limiting current density, neglecting the effects of other factors (such as the effect of the pore radius on effective electrochemical surface area, which can affect the reaction rate of ORR and current density). All these results indicate that there exists an optimal radius of order-structured CLs by achieving a balance between electrochemical reaction properties and mass transport properties.

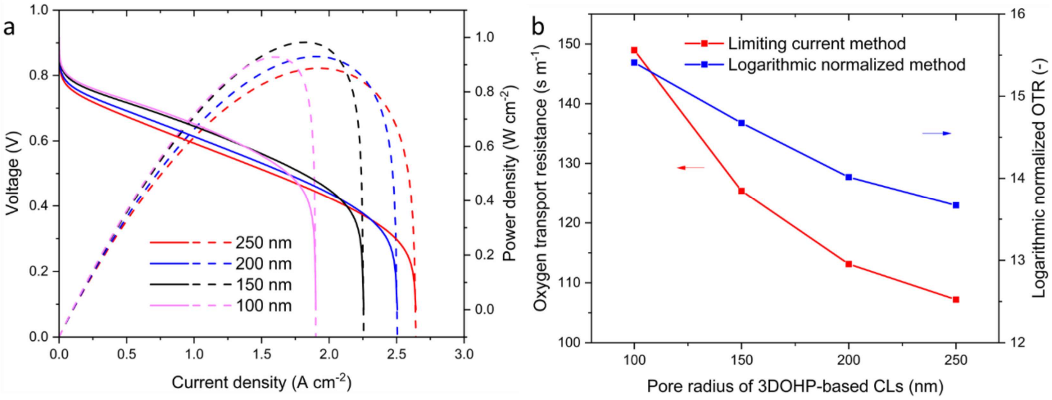

Fig. 9. Effect of pore size of order-structured CLs on (a) PEMFC performance and (b) Local oxygen transport resistances. Operating voltage: 0 V, Pt loading: 0.12 mg cm^{-2}.

4.4. Effect of relative humidity

Relative humidity plays a critical role in determining the PEMFC performance as it affects the proton conductivity of proton exchange membrane and ionomer as well as two-phase mass transport in porous media. To elucidate the effect of relative humidity on performance of PEMFCs with order-structured CLs, the polarization curves of PEMFCs and OTRs under different relative humidity are compared. As shown in Fig. 10a, the PEMFC exhibits the best performance at 80% relative humidity, achieving a limiting current density of 3.46 A cm^{-2} and peak power density of 0.88 W cm^{-2}. When relative humidity is decreased from 100% to 80%, the average saturation is reduced by 38%, resulting in higher effective diffusion coefficient in the cathode porous media, which facilitates bulk oxygen transport. When relative humidity is reduced further (from 70% to 50%), it is found in Fig. 10a that the ohmic polarization is increased significantly, because the proton conductivity of PEM is decreased due to low hydration in low humidity. Meanwhile, the concentration polarization in low relative humidity is not obvious, because oxygen supply in CLs is sufficient when current density is low. Thus, polarization results indicate that the optimal relative humidity for PEMFCs with order-structured CLs is 80%, under which the mass transport kinetics and ohmic loss are compromised.

It can be seen in Fig. 10b that OTRs calculated by the logarithmic normalized method and the limiting current method show an opposite trend when varying relative humidity. The logarithmic normalized OTRs increase significantly when increasing relative humidity.

However, OTRs revealed by the limiting current method are decreased when relative humidity is increased, because the limiting current density is significantly increased. From the abovementioned discussion of polarization curves in different relative humidity, it is concluded that OTRs are reduced when decreasing relative humidity. Herein, OTRs calculated by our proposed logarithmic normalized method shows the identical tendency, but the conventional limiting current method does not. In the conventional limiting current method, OTRs defined by the limiting current method are determined by the limiting current density, when $C_{O_2,CH}$ is kept as constant in Eq. (47). In this regard, other factors which can significantly affect cell performance are neglected. (e.g., effect of humidity on proton conductivity of PEM and effect of temperature on electrokinetics). Thus, the limiting current method is improper to describe the effect of humidity on mass transport. The comparison in Fig. 10b exhibits the superiority of our proposed logarithmic normalized method for calculating OTRs in comparison to the conventional limiting current method.

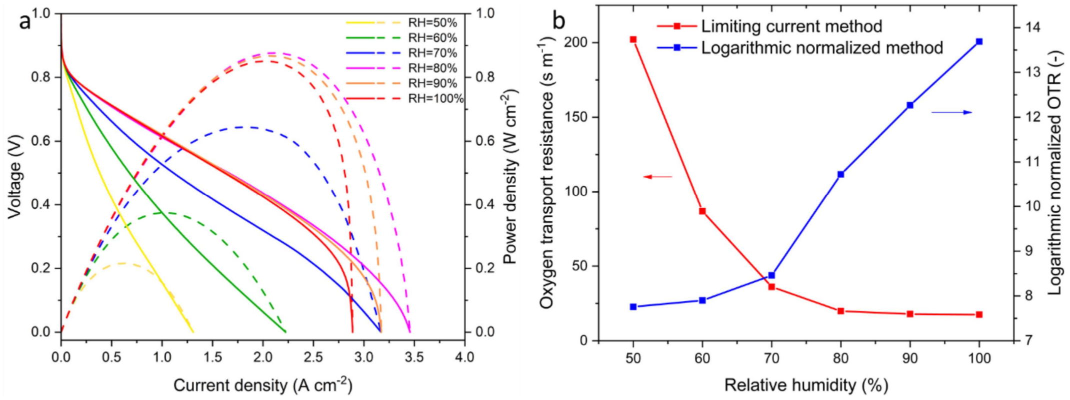

Fig. 10. Effect of relative humidity on (a) PEMFC performance and (b) Local oxygen transport resistances. Operating voltage: 0 V, Pt loading: 0.12 mg cm^{-2}.

5. Conclusion

In summary, a multiscale model is successfully developed to investigate the mass transport characteristics and cell performance of PEMFCs with order-structured CLs. The multiscale model is validated by experimental results from the literature and can be extended to various types of CLs with ordered structures. Our results show that PEMFCs with order-structured CLs exhibit superior performance than those with the conventional ones, due to the enhanced bulk and local oxygen transport. To further analyze the local oxygen transport characteristics under both limiting and non-limiting current conditions, a logarithmic normalized method is proposed. It is found that local OTRs show an inverse proportional function of Pt loading and increase dramatically when the Pt loading is lower than 0.10 mg cm^{-2}. Under the non-limiting current conditions, both the ionomer-Pt interfacial resistance and ionomer diffusive resistance increase remarkably when decreasing voltage from 0.45 to 0 V. Under the limiting current conditions, the local oxygen concentration on Pt surface is approaching zero, leading to weak adsorption of oxygen on Pt surface and thus a big ionomer-Pt interfacial resistance. The ionomer-Pt interfacial resistance is dominant among all the local OTRs. In addition, the radius of 3DOHP-based CLs and relative humidity are optimized to balance the reactive surface area, oxygen transport resistance, and proton conductivity of membrane and ionomer, thereby achieving optimal cell performance.

Acknowledgment

The work described in this paper was supported by HKUST Fund of Foshan (Grant No. FSUST19-FYTRI06).

References

[1] D.A. Cullen, K.C. Neyerlin, R.K. Ahluwalia, R. Mukundan, K.L. More, R.L. Borup, A.Z. Weber, D.J. Myers, A. Kusoglu, New roads and challenges for fuel cells in heavy-duty transportation, Nat. Energy. 6 (2021) 462–474.

[2] M.K. Debe, Electrocatalyst approaches and challenges for automotive fuel cells, Nature. 486 (2012) 43–51.

[3] K. Jiao, J. Xuan, Q. Du, Z. Bao, B. Xie, B. Wang, Y. Zhao, L. Fan, H. Wang, Z. Hou, others, Designing the next generation of proton-exchange membrane fuel cells, Nature. 595 (2021) 361–369.

[4] S.T. Thompson, D. Papageorgopoulos, Platinum group metal-free catalysts boost cost competitiveness of fuel cell vehicles, Nat. Catal. 2 (2019) 558–561.

[5] T. Jahnke, G. Futter, A. Latz, T. Malkow, G. Papakonstantinou, G. Tsotridis, P. Schott, M. Gérard, M. Quinaud, M. Quiroga, others, Performance and degradation of Proton Exchange Membrane Fuel Cells: State of the art in modeling from atomistic to system scale, J. Power Sources. 304 (2016) 207–233.

[6] T.A. Greszler, D. Caulk, P. Sinha, The impact of platinum loading on oxygen transport resistance, J. Electrochem. Soc. 159 (2012) F831.

[7] N. Nonoyama, S. Okazaki, A.Z. Weber, Y. Ikogi, T. Yoshida, Analysis of oxygen-transport diffusion resistance in proton-exchange-membrane fuel cells, J. Electrochem. Soc. 158 (2011) B416.

[8] A.Z. Weber, A. Kusoglu, Unexplained transport resistances for low-loaded fuel-cell catalyst layers, J. Mater. Chem. A. 2 (2014) 17207–17211.

[9] J.M. Kim, J.-H. Kim, J. Kim, Y. Lim, Y. Kim, A. Alam, J. Lee, H. Ju, H.C. Ham, J.Y. Kim, Synergetic structural transformation of Pt electrocatalyst into advanced 3D

architectures for hydrogen fuel cells, Adv. Mater. 32 (2020) 2002210.

[10] M.K. Debe, Tutorial on the fundamental characteristics and practical properties of nanostructured thin film (NSTF) catalysts, J. Electrochem. Soc. 160 (2013) F522.

[11] Z.Q. Tian, S.H. Lim, C.K. Poh, Z. Tang, Z. Xia, Z. Luo, P.K. Shen, D. Chua, Y.P. Feng, Z. Shen, others, A highly order-structured membrane electrode assembly with vertically aligned carbon nanotubes for ultra-low Pt loading PEM fuel cells, Adv. Energy Mater. 1 (2011) 1205–1214.

[12] S. Murata, M. Imanishi, S. Hasegawa, R. Namba, Vertically aligned carbon nanotube electrodes for high current density operating proton exchange membrane fuel cells, J. Power Sources. 253 (2014) 104–113.

[13] Z. Zhu, H. Yin, Y. Wang, C.-H. Chuang, L. Xing, M. Dong, Y.-R. Lu, G. Casillas-Garcia, Y. Zheng, S. Chen, others, Coexisting Single-Atomic Fe and Ni Sites on Hierarchically Ordered Porous Carbon as a Highly Efficient ORR Electrocatalyst, Adv. Mater. 32 (2020) 2004670.

[14] K. Shen, L. Zhang, X. Chen, L. Liu, D. Zhang, Y. Han, J. Chen, J. Long, R. Luque, Y. Li, others, Ordered macro-microporous metal-organic framework single crystals, Science (80-.). 359 (2018) 206–210.

[15] O.-H. Kim, Y.-H. Cho, S.H. Kang, H.-Y. Park, M. Kim, J.W. Lim, D.Y. Chung, M.J. Lee, H. Choe, Y.-E. Sung, Ordered macroporous platinum electrode and enhanced mass transfer in fuel cells using inverse opal structure, Nat. Commun. 4 (2013) 1–9.

[16] A.Z. Weber, R.L. Borup, R.M. Darling, P.K. Das, T.J. Dursch, W. Gu, D. Harvey, A. Kusoglu, S. Litster, M.M. Mench, others, A critical review of modeling transport phenomena in polymer-electrolyte fuel cells, J. Electrochem. Soc. 161 (2014) F1254.

[17] S.M. Rao, Y. Xing, Simulation of nanostructured electrodes for polymer electrolyte membrane fuel cells, J. Power Sources. 185 (2008) 1094–1100.

[18] M.M. Hussain, D. Song, Z.-S. Liu, Z. Xie, Modeling an ordered nanostructured cathode catalyst layer for proton exchange membrane fuel cells, J. Power Sources. 196 (2011) 4533–4544.

[19] L. Liang, Y. Wei, X. Zhang, S. Chen, F. Yu, Z.Q. Tian, P.K. Shen, 3D model of an order-structured cathode catalyst layer with vertically aligned carbon nanotubes for PEM fuel cells under the water flooding condition, ACS Sustain. Chem. \& Eng. 8 (2019) 695–705.

[20] I. V Zenyuk, P.K. Das, A.Z. Weber, Understanding impacts of catalyst-layer thickness on fuel-cell performance via mathematical modeling, J. Electrochem. Soc. 163 (2016) F691.

[21] G. Zhang, J. Wu, Y. Wang, Y. Yin, K. Jiao, Investigation of current density spatial distribution in PEM fuel cells using a comprehensively validated multi-phase non-isothermal model, Int. J. Heat Mass Transf. 150 (2020) 119294.

[22] J. Liang, Y. Li, R. Wang, J. Jiang, Cross-dimensional model of the oxygen transport behavior in low-Pt proton exchange membrane fuel cells, Chem. Eng. J. 400 (2020) 125796.

[23] B. Xie, G. Zhang, J. Xuan, K. Jiao, Three-dimensional multi-phase model of PEM fuel

cell coupled with improved agglomerate sub-model of catalyst layer, Energy Convers. Manag. 199 (2019) 112051.

[24] L. Hao, K. Moriyama, W. Gu, C.-Y. Wang, Modeling and experimental validation of Pt loading and electrode composition effects in PEM fuel cells, J. Electrochem. Soc. 162 (2015) F854.

[25] R. Vetter, J.O. Schumacher, Free open reference implementation of a two-phase PEM fuel cell model, Comput. Phys. Commun. 234 (2019) 223–234.

[26] R. Vetter, J.O. Schumacher, Experimental parameter uncertainty in proton exchange membrane fuel cell modeling. Part I: Scatter in material parameterization, J. Power Sources. 438 (2019) 227018.

[27] W.W. Yang, T.S. Zhao, A two-dimensional, two-phase mass transport model for liquid-feed DMFCs, Electrochim. Acta. 52 (2007) 6125–6140.

[28] N.P. Subramanian, T.A. Greszler, J. Zhang, W. Gu, R. Makharia, Pt-oxide coverage-dependent oxygen reduction reaction (ORR) kinetics, J. Electrochem. Soc. 159 (2012) B531.

[29] Q. Zhao, P. Majsztrik, J. Benziger, Diffusion and interfacial transport of water in Nafion, J. Phys. Chem. B. 115 (2011) 2717–2727.

[30] R. Jinnouchi, K. Kudo, N. Kitano, Y. Morimoto, Molecular dynamics simulations on O2 permeation through nafion ionomer on platinum surface, Electrochim. Acta. 188 (2016) 767–776.

[31] Y. Kurihara, T. Mabuchi, T. Tokumasu, Molecular dynamics study of oxygen transport resistance through ionomer thin film on Pt surface, J. Power Sources. 414 (2019) 263–271.

[32] S. Shen, X. Cheng, C. Wang, X. Yan, C. Ke, J. Yin, J. Zhang, Exploration of significant influences of the operating conditions on the local O 2 transport in proton exchange membrane fuel cells (PEMFCs), Phys. Chem. Chem. Phys. 19 (2017) 26221–26229.

[33] J.P. Meyers, R.M. Darling, Model of carbon corrosion in PEM fuel cells, J. Electrochem. Soc. 153 (2006) A1432.

[34] T. Wilberforce, Z. El-Hassan, F.N. Khatib, A. Al Makky, A. Baroutaji, J.G. Carton, J. Thompson, A.G. Olabi, Modelling and simulation of Proton Exchange Membrane fuel cell with serpentine bipolar plate using MATLAB, Int. J. Hydrogen Energy. 42 (2017) 25639–25662.

[35] G.N. Derry, P.N. Ross, A work function change study of oxygen adsorption on Pt (111) and Pt (100), J. Chem. Phys. 82 (1985) 2772–2778.

[36] G. Lin, W. He, T. Van Nguyen, Modeling liquid water effects in the gas diffusion and catalyst layers of the cathode of a PEM fuel cell, J. Electrochem. Soc. 151 (2004) A1999.

[37] A. Kongkanand, M.F. Mathias, The priority and challenge of high-power performance of low-platinum proton-exchange membrane fuel cells, J. Phys. Chem. Lett. 7 (2016) 1127–1137.